LA-UR-15-22292
Approved for public release; distribution is unlimited.

Title: Mitigating cutting-induced plasticity in the contour method. Part 2: Numerical analysis

Author(s): Muransky, Ondrej
Hamelin, Cory J
Hosseinzadeh, Foroogh
Prime, Michael Bruce

Intended for:

Issued: 2015-03-31

Final reference:

Muránsky, O., Hamelin, C. J., Hosseinzadeh, F., and Prime, M. B., 2016, "Mitigating cutting-induced plasticity in the contour method. Part 2: Numerical analysis," International Journal of Solids and Structures, 94–95, pp. 254-262.

http://dx.doi.org/10.1016/j.ijsolstr.2015.12.033

Mitigating Cutting-Induced Plasticity in the Contour Method, Part 2: Numerical Analysis

O. Muránsky[1], C.J. Hamelin[1], F. Hosseinzadeh[2], M.B. Prime[3]

[1] ANSTO, Institute of Materials Engineering, Lucas Heights, NSW, Australia
[2] Open University, Materials Engineering, Milton Keynes, MK7 7AA, UK
[3] Los Alamos National Laboratory, Los Alamos, NM 87545, USA

Abstract

Cutting-induced plasticity can have a significant effect on the measurement accuracy of the contour method. The present study examines the benefit of a double-embedded cutting configuration that relies on self-restraint of the specimen, relative to conventional edge-crack cutting configurations. A series of finite element analyses are used to simulate the planar sectioning performed during double-embedded and conventional edge-crack contour cutting configurations. The results of numerical analyses are first compared to measured results to validate the cutting simulations. The simulations are then used to compare the efficacy of different cutting configurations by predicting the deviation of the residual stress profile from an original (pre-cutting) reference stress field, and the extent of cutting-induced plasticity. Comparisons reveal that while the double-embedded cutting configuration produces the most accurate residual stress measurements, the highest levels of plastic flow are generated in this process. This cutting-induced plastic deformation is, however, largely confined to small ligaments formed as a consequence of the sample sectioning process, and as such it does not significantly affect the back-calculated residual stress field.

Keywords: Residual stress, Contour method, Finite element modelling

Tel.: +61 (0)2 9717 3488, **Fax.:** +61 (0)2 9543 7179, **E-mail:** ondrej.muransky@ansto.gov.au

1. Introduction

One of the most recently developed residual stress measurement techniques is the contour cutting method [1-4], which is based on a variation of Bueckner's principle [5] of elastic superposition. The contour method is a "destructive"[1] stress-relief method that is performed in four stages: (i) planar sectioning of the specimen along the region of interest; (ii) measurement of the resultant out-of-plane deformation caused by the relief of internal residual stresses; (iii) post-processing of the measured data (i.e. 2D data smoothing/fitting); and (iv) numerical back-calculation of initial residual stresses using finite element (FE) analysis. In this final stage, the sectioned specimen geometry is uploaded into a fully elastic FE model, and the measured out-of-plane displacement is applied as a displacement boundary condition. The original (pre-cutting) residual stress field in the specimen is thus recovered using FE linear elastic stress analysis. A primary advantage of the technique is that it is insensitive to any microstructural changes that often arise between weld and parent metal, as well as the ability to measure very thick specimens [6-8]. The required equipment is also readily available and easy-to-use when compared to "non-destructive"[2] (e.g. diffraction) techniques [9]. On the other hand, the contour cutting method is limited in that only one stress component (perpendicular to the cutting surface) can be determined from a single cut unless additional techniques or multiple cuts are also used [10].

While planar sectioning of the specimen using electric discharge machining (EDM) is straightforward relative to diffraction techniques, the accuracy of the contour method is dependent upon a number of theoretical assumptions inherent to its methodology [1, 11]. Measurement errors can be divided into "symmetric" and "anti-symmetric" components [11]. Anti-symmetric errors are often caused by residual shear stresses in the sample or by crooked cutting; these errors can be removed by averaging the measured out-of-plane deformation on both cutting surfaces [11]. In contrast, symmetric errors that depend on the magnitude of residual stresses[3] in the sample can be caused by *plastic flow* during cutting [3, 11-13] and so-called *bulge* [11]; these errors cannot be corrected after the cut is performed. Metal plasticity introduced during the cutting procedure is one of the biggest challenges in achieving accurate residual stress measurements. Traditionally, researchers have attempted to mitigate this source of error through significant clamping of the specimen during cutting [11, 14-17], to varying degrees of success. Clamping is intended to minimise the transient stress redistribution caused by the introduction of a free surface in the specimen during cutting, so that these transient stresses do not exceed the yield strength of the material.

Rather than relying on significant clamping of the specimen during cutting, a novel double-embedded cutting configuration has been proposed to minimise cutting-induced plasticity during the cutting process. This procedure takes advantage of self-constraint of the specimen, and is a stress-informed cutting configuration in that the length and direction of each cut is made based on the assumed residual stresses in the component. Part 1 of the present study [18] elucidates the rationale behind this novel cutting configuration, based on

[1] The original internal residual stress field in the specimen is released during the measurement process, and cannot be remeasured using complementary techniques.
[2] The original internal residual stress field in the specimen is preserved during the measurement process; however, the extraction of a reference stress-free coupon from this or another specimen is often required.
[3] There are some symmetric errors that do not depend on the magnitude of residual stress in the sample. These errors can be corrected by an offset of the measured contour [11].

the results obtained from a three-pass austenitic steel weld specimen. Part 2 (the present paper) quantitatively examines the benefit of a double-embedded cutting configuration for the minimisation of cutting-induced plasticity by means of numerical parametric analysis. The experimental results from Part 1 [18] are reproduced numerically using a validated weld FE model previously developed for this benchmark weld specimen [19]. The stress predictions from this configuration are then compared to the predicted weld residual stresses (WRS) recovered using conventional edge-crack contour cutting configurations that assume (i) minimal constraint is present during the cutting process, and (ii) traditional clamping is used during the cutting process. The use of a validated weld FE model in this fashion provides a rare opportunity to quantify the benefit of a given contour cutting configuration, and may serve in the future as an optimisation tool for the contour method stress measurement community.

2. Benchmark specimen and residual stress measurement

One of the most common applications of residual stress measurement involves welded metallic structures [20], owing to the reduced service lifetimes of welded components caused by WRS. In an effort to improve WRS prediction and measurement techniques, a task group (TG4) has been established by the European Network on Neutron Techniques Standardisation for Structural Integrity (NeT). Within NeT TG4, the WRS in a three-pass slot weld in AISI 316LN austenitic steel was measured using a variety of techniques, and predicted using FE simulation of the welding process. A series of benchmark weld specimens were manufactured using an identical weld procedure, ensuring process repeatability and allowing simultaneous WRS measurement as part of the international round-robin study. The weld design comprises a three-pass ER316L austenitic steel slot weld in solution heat-treated AISI 316LN austenitic steel plate. The nominal dimensions of the plate, shown in Fig. 1a, are ($150 \times 18 \times 194$) mm with an 80-mm long and 6-mm deep centreline slot. The slot was filled with three superimposed weld passes via a mechanised Tungsten Inert Gas (TIG) welding process.

In terms of contour method measurements, previous studies [19, 21] identified the longitudinal WRS profile to be the most significant in the NeT TG4 samples; therefore, cross-weld planar sectioning (Fig. 1a) was performed to measure these stresses. Since a standard contour method will provide a single stress component, only the longitudinal stress field will be measured. However, for most welding applications it is the longitudinal WRS that are of greatest importance, and they are the focus of this work.

3. Numerical analysis

Numerical (FE) analysis is split into two components. First the predicted WRS in the NeT TG4 specimens were validated against diffraction measurements [19]. Then numerical simulation of the contour cutting method was conducted and validated against the recovered (back-calculated) WRS measured from the double-embedded contour method [18]. Alternate cutting methods were then simulated, and the results compared to assess the efficacy of the double-embedded cutting procedure to recover original (pre-cutting) WRS. The following sections highlight the specifics of each modelling effort.

3.1 Prediction of weld residual stresses

The WRS in the NeT TG4 weld specimens have been predicted [21, 22] via 3D moving heat-source welding simulations developed using the ABAQUS commercial FE package [23]. A 3D half-model was employed (schematically shown in Fig. 1a) to take advantage of sample and process symmetry about the weld centreline, thus dramatically improving the computational efficiency of the simulation. The material deposition of three consecutive passes was handled by ABAQUS element activation, adding weld material from each of the weld passes as an independent element set. The heat source was calibrated using a dedicated FEAT-WMT package [19], which employs a steady-state 3D moving mesh solution with a Gaussian ellipsoidal heat source to be calibrated against the measured weld fusion zone and thermocouple readings [19]. FEAT-WMT defines the heat source as a body heat flux, which is then imported to the ABAQUS as a series of time- and spatially-resolved volumetric power densities via a DFLUX subroutine. A sequentially coupled thermo-mechanical FE analysis was then performed, whereby the numerical solution from the thermal FE analysis was used as an input for the mechanical FE analysis. The thermal and mechanical models comprise 38,220 hexahedral quadratic elements, however, the element types are dependent on the simulation performed: thermal analysis used quadratic heat transfer elements (ABAQUS designation DC3D20) while mechanical analysis used reduced-integration quadratic stress elements (ABAQUS designation C3D20R).

It is likely that abundance of high-temperature δ-ferrite is present in the molten weld pool; however, most of this δ-ferrite transforms back to austenite at temperatures close to the melting point of the material (well above annealing temperature) thus having negligible effect on the final WRS. The presence of this high-temperature solid-state phase transformation was therefore not considered in the present weld modelling simulations. Even though the parent (316LN) and filler (ER316L) metals have a slightly different chemical composition [19], the same physical[4] and elasto-plastic[5] mechanical properties were used for both materials over the temperature range of interest (20°C – 1500°C) [19]. In order to accurately capture the welding-induced work-hardening of the material, a mixed isotropic-kinematic plasticity model has been identified [21] as the most appropriate. The loss of isotropic work-hardening at high temperatures was modelled by setting the ABAQUS annealing temperature to 1050°C, thus resetting the size of the yield surface to an undeformed, temperature-dependent shape when annealing occurs.

All WRS predictions are presented in Ref. [19] alongside neutron and synchrotron X-ray diffraction measurements. A set of measured and predicted cross-weld line profiles from this work are presented in Fig. 2. Note that the half-model results have been reflected about the weld centreline, in accordance with symmetry assumptions. Even though the model over-predicts the longitudinal WRS in the weld metal region (Fig. 2c) [19, 21] a good overall agreement between the predictions and two independent diffraction measurements validate the weld FE model. This validation is vital to ensure that any major inaccuracies observed in the subsequent contour method simulations are not the result of pre-existing errors in the input weld model results. The measurement and FE predictions confirm high levels (~ 400 MPa) of tensile longitudinal WRS in the vicinity of the weld heat affected zone (HAZ). Note that the room-temperature yield stress of the annealed parent metal is only 125 MPa, which implies that the near-weld material experiences significant welding-induced work-hardening during the welding process [19, 21].

[4] Density (ρ), thermal conductivity (λ), and specific heat (c_p).

[5] Young's modulus (E), Poisson's ratio (ν), and work-hardening behaviour.

3.2 Prediction of cutting-induced plasticity

The FE model developed to simulate contour cutting procedures requires the full WRS and strain tensors obtained by the numerical FE weld simulation as input. This model represents the initial, uncut reference state of the NeT TG4 benchmark weld specimen. This data was mapped onto a contour cutting FE model in several stages, as shown in Fig. 3. The following mapping procedure was followed:

1. Figure 3a shows the predicted longitudinal (σ_{33}) WRS on the cross-weld plane at the specimen mid-length (i.e. plane-of-cut in Fig. 1a), for the distorted geometry predicted by the weld FE model [19, 21]. Omission of the welding-induced distortion is desired to simplify the contour cutting simulation; it is therefore assumed that the pre-existing distortion of the benchmark specimen has no significant effect on the contour measurements. The distortion was omitted by running an additional mechanical analysis step after the weld simulation, wherein the nodal displacements were not recorded. This undeformed WRS profile (stress map), shown in Fig. 3b, is identical to the profile obtained from the distorted geometry (no significant modification of WRS is thus introduced from this omission of welding-induced distortion).

2. While the welding process is symmetric about the weld centreline, the contour cutting procedure is not. Therefore, a full 3D model is required such that the symmetric predictions shown in Fig. 3b had to be mirrored about the symmetry plane and mapped onto a full 3D contour cutting FE model (Fig. 1). Because a greater level of numerical accuracy is required near the cross-weld cut surface for the contour cutting simulation, the original mesh used for the weld FE model was significantly refined. A fine mesh was constructed in and near the contour cut region as it is shown in Fig. 1b. The total number of elements (C3D20R) increased from 38,220 in the weld half-model to 396,626 in the full 3D contour cutting model. Fig. 3c and Fig. 3d show predicted post-weld longitudinal residual stress (σ_{33}), and longitudinal plastic strain ($\varepsilon_{33}^{pl.}$) mirrored about the symmetry plane on an undistorted full 3D contour cutting FE model.

3. A 0.32-mm[6] wide section of material was removed along the cutting plane to simulate the EDM cutting process. Therefore, a series of (0.32×0.32×18) mm through-thickness element sets were sequentially removed to simulate the cutting process as shown schematically in Fig. 1a. This approach was applied to all cutting configurations (i.e. all cuts applied for double-embedded and single edge-crack analyses). Since the cutting rate is not assumed to influence the metal plasticity observed, an arbitrary advance rate of 0.32 mm/s was used (i.e. one element set was removed each 1-s increment of the analysis). Rate-independent material properties were also used to eliminate any strain-rate effects that may arise due to this arbitrary cutting speed.

[6] The width of the cut section in the FE simulations accounts for the wire diameter of 0.25mm and removed (evaporated) material. The width of the cut section was kept constant in all FE models for the sake of consistency in the performed numerical parametric analysis. Actual measurements employing the double-embedded cutting configuration (represented by Model A) used 0.15-mm diameter wire [18].

4. Once planar sectioning was simulated, the predicted out-of-plane displacement on both cut surfaces was averaged, and used in a new fully elastic FE model of the cut specimen to back-calculate the original pre-cutting WRS. This process is identical to the procedure used in the experimental contour cutting method described in Part 1 of the present study [18], where the longitudinal WRS are back-calculated assuming an elastic material response due to stress relaxation during cutting. If plasticity would not occur during the cutting process, the original and back-calculated (recovered) stress fields would be the same based on Bueckner's principle [5] of elastic superposition.

In order to investigate the effect of different cutting configurations on the cutting-induced metal plasticity, three models were constructed with different prescribed boundary conditions. These models are schematically shown in Fig. 4. A brief description of the boundary conditions used in each model is given below.

Model A: The double-embedded cutting procedure uses two pilot holes to split the planar sectioning operation into 4 separate cuts, as shown in Fig. 4a. The first cut starts from one pilot hole[7], progressing inwards for 75 mm along the plane-of-cut and terminating at the far end of the weld bead. This cut is followed by a second cut (65 mm) that originates at the second pilot hole, travelling inwards until the free surface generated by the first cut is met. The cutting process is then finished by removing the two remaining 5-mm ligaments (third and fourth cuts) on both sides of the specimen in the same manner (i.e. one element set per second). Because the specimen is largely self-constrained during the cutting process, the model was only prevented from rigid-body rotation using pin constraints, as shown in Fig. 1a and Fig. 4a. Note that during the actual cutting process, light clamping was used to prevent rigid-body movement.

Model B: This model possesses the same pin-constraint boundary conditions as in Model A to prevent rigid body rotation; however, the model was sectioned in a single cut, as shown in Fig. 4b. No pilot holes were used, so there was relatively little self-constraint whilst cutting. This constraint case should be similar to the case of clamping on only one side of the cut, which is not recommended [11] but is occasionally used so that an incremental slitting measurement [24] can be carried out simultaneously with the contour method [25, 26].

Model C: As with Model B, this model was sectioned in a single cut but here a set of rigid clamps were applied as shown in Fig. 4c. This model represents a more conventional contour cutting configuration where the cutting-induced plasticity is reduced by secure clamping of the specimen. These simulated clamps are highly conservative, i.e. they completely prohibit any movement of the underlying material; in practice it is assumed that some slippage would occur. It should also be noted that the size and location of the clamps used have not been optimised and cutting-induced plasticity may be further mitigated upon clamp optimisation.

4. Results and Discussion

[7] In order to simplify the geometry and improve mesh quality the pilot holes were modelled by removal of through-thickness squared sections (i.e. hole geometry was idealised).

The original (pre-cutting) WRS in the NeT TG4 weld specimen as measured by diffraction techniques and predicted by FE weld simulation are shown in Fig. 2 and Fig. 3. Measured and predicted WRS are in good agreement despite noticeable over-prediction of longitudinal (σ_{33}) WRS in the weld metal region (see Ref. [19, 21] for details), which implies the analyst may be confident that any error in subsequent validation of contour cutting simulations is not caused by an inaccuracy in WRS data input.

The predicted longitudinal WRS along the plate mid-thickness when simulating the double-embedded cutting configuration on the TG4 weld model is presented in Fig. 5b. Details of the efficacy of this cutting configuration in capturing the original WRS are discussed in Part 1 [18] of this study. However, it is apparent from a comparison of measured and predicted WRS results that the double-embedded contour cutting FE model is valid for simulating cutting-induced plasticity. Since we can be confident in our numerical solutions, we can now compare the predicted WRS profiles produced using different cutting configurations, and compare those profiles against the predicted pre-cutting WRS in the NeT TG4 specimen to determine the efficacy of each configuration.

Figures 5c and 5d present the predictions of recovered WRS by the contour method employing a conventional edge-crack configuration (Models B and C, respectively). Using the predicted WRS in the NeT TG4 specimen (Fig. 3c) as a basis of comparison, it becomes apparent that the WRS recovered by contour cutting configurations employing edge-crack configurations are less accurate than the double-embedded configuration. In particular, a greater asymmetry of the recovered WRS field exists when using these edge-crack procedures, which implies double-embedded procedures are more effective in mitigating the influence of cutting-induced plasticity.

To better understand the key features affecting the recovered WRS for each cutting configuration, the cutting-induced plasticity has been calculated. This calculation was carried out by subtracting the longitudinal welding-induced plasticity predicted in Fig. 3d from the post-cutting longitudinal plastic strain predicted in each contour cutting simulation. Note that the final plastic strain accumulated in the cut specimen comprises both the welding-induced plasticity and cutting-induced plasticity, thus requiring a decoupling procedure. The longitudinal cutting-induced plasticity (ε_{33}^{pl}) calculated for Models A, B and C is presented in Fig. 6. Line profiles of this cutting-induced plastic strain along the sample mid-thickness (Line B9 as shown in Fig. 1a) are compared in Fig. 6a. It is clear that the largest values of plastic strain are accumulated during the double-embedded cutting procedure, throughout the regions highlighted in Fig. 6b[8]. However, Fig. 6 shows that a compressive ε_{33}^{pl} is concentrated near the pilot holes and tensile ε_{33}^{pl} is observed in the material remaining near the end of the second cut (i.e. where the first and second cuts meet). These high levels of metal plasticity are caused by the local stress concentration that occurs within the relatively small material ligaments formed along the plane-of-cut, compounded by stress redistribution in the sample during the cutting process. Use of pilot holes creates 5-mm long ligaments at either end of the specimen (see Fig. 4a). These ligaments experience high compressive stress levels due to transient WRS redistribution during the cutting process. A similar event occurs during the second inward cut (cut 2 in Fig.

[8] Note that the upper-bound plastic strain shown in Fig. 6b is capped at -1.0% and 1.0%, to directly compare cutting-induced plasticity trends with those observed in Models B and C. For clarity, the actual upper-bound strains are included in Fig. 6a.

6a) since an increasingly smaller ligament is formed as the EDM wire travels towards the free surface created by the first cut. Hence, WRS redistribution causes local tensile stresses to increase as the ligament length decreases, until they exceed the yield strength of the material. High levels of metal plasticity are therefore achieved as the second cut nears completion.

The effect of cutting-induced plasticity on recovered WRS can be somewhat clearer when looking at predicted out-of-plane displacement, which is a consequence of both elastic and plastic strain released during cutting process. Fig. 7 shows averaged (over both cutting surfaces) out-of-plane displacement in all FE nodes on the cutting surface as predicted by Models A, B and C, in direct comparison to predicted fully elastic out-of-plane displacement in an idealised elastic model. Note that if this idealised, fully elastic out-of-plane displacement is used in WRS back-calculation it would lead to recovery of the exact original (pre-cutting) WRS shown in Fig. 3c. The closer the out-of-plane displacement profile comes to the out-of-plane displacement in this idealised elastic model, the more accurate are the recovered (back-calculated) WRS.

It becomes clear from Fig. 7a that the localisation of cutting-induced plasticity near the pilot holes and the material remaining near the end of the second inward cut causes large localised displacement. It is also apparent that this localised plastic flow has limited effect on the overall out-of-plane displacement profile over the cutting plane. If we would neglect these localised features the out-of-plane displacement predicted by Model A would closely follow that of the idealised elastic displacement. It stands to reason that because these regions of localised large displacements are not caused by elastic deformation (i.e. elastic relaxation of WRS field), they should be eliminated from the WRS back-calculation process (Part 1 [18]). Hence, the out-of-plane displacement recorded when using the double-embedded cutting configuration was removed at both edges and near the end of second inward cut as shown in Fig. 7a. The displacement data were then interpolated through the gap created by omitting those data points as shown in Fig. 7b. This procedure is justifiable since these local features in the out-of-plane displacement profile are at locations that can be reasonably assumed to be anomalous because of the ligaments formed. It is common procedure to remove apparent cutting artefacts from the data when an artefact is so localized that it could not come from elastic stress relaxation [27]. The post-processed out-of-plane displacement data are then used in the back-calculation of WRS (Fig. 5b). The same procedure is used for the measurements obtained using the double-embedded cutting configuration (Fig. 5a).

In contrast to these concentrated regions of plastic flow, the cutting-induced plasticity predicted in Models B and C are more diffuse as shown in Figs. 6c and 6d, respectively. For Model B, the lack of clamping causes a more significant WRS redistribution and metal plasticity during the first half of the cut, which leads to the inaccurate WRS predictions shown in Fig. 5c. In the latter half of the cut, transient WRS redistribution does not lead to metal plasticity since most of the redistribution (relaxation) has already occurred. The recovered WRS predictions in this half of the specimen are thus more accurate as indicated by the out-of-plane deformation shown in Fig. 7c. In the case of a clamped specimen arrangement (Model C), WRS redistribution is marginalised during the first half of the cutting process (Fig. 7d). As a result, the cutting-induced plasticity is lower and the WRS predictions in Fig. 5d are more accurate than those predicted from an unconstrained geometry. However, since WRS redistribution is prevented during the first half of the cut by

rigid clamping, the high tensile stresses that remain near the weld fusion zone and HAZ create local metal plasticity during the second half of the cutting process. Remnant WRS due to clamping also leads to a similar “ligament plasticity” near the end of the cut as observed in the self-constrained Model A results.

Even though the recovered WRS predictions in Models A and C are not too dissimilar, one needs to remember that the rigid clamping assumed for Model C has been idealised, and is difficult to achieve in practice. It is thus far more practical to use an embedded cutting configuration, which requires only light clamping to prevent rigid body rotation during the cutting process and relies on specimen self-constraint. Furthermore, using a stress-informed double-embedded cutting configuration will further mitigate plastic flow during the cutting process, leading to greater accuracy in the recovered WRS.

5. Conclusions

Cutting-induced plasticity can have a significant effect on the measurement accuracy of the contour cutting method. The present study examines the efficacy of a novel double-embedded cutting configuration, relative to more traditional edge-crack configurations. This study benefits from the use of a validated weld FE model, which accurately captures the WRS in the NeT TG4 weld benchmark specimen and has been used for comparative analyses. The following observations have been made:

- Comparison of measured and predicted WRS when using the double-embedded cutting procedure are in good agreement. The FE approach used to simulate planar sectioning has therefore been validated, and the findings of the subsequent comparative study can be considered sound.
- Longitudinal WRS produced using a double-embedded cutting configuration captures the original (i.e. welding-induced) WRS more accurately than the more traditional edge-crack configurations. This procedure is advantageous since it relies on specimen self-constraint, and minimal clamping is required.
- The peak magnitude of predicted cutting-induced plasticity is higher for the double-embedded cutting configuration than for the edge-crack configurations. These high levels of plasticity are, however, concentrated within regions where ligaments are formed during the cutting process (i.e. outside each pilot hole, and between the second and first cut as the second cut nears completion). Transient WRS redistribution during the cutting process creates stress concentrations in these regions that lead to plastic flow. Due to the localised nature of plastic flow when using a double-embedded cutting configuration, the cutting-induced plasticity has a limited influence on the overall out-of-plane displacement and thus recovered (back-calculated) WRS.
- While peak cutting-induced plasticity is not as severe in edge-crack processes, plastic flow occurs over a greater amount of material, leading to less accurate measurements of WRS over the plane-of-cut. For the unclamped edge-crack procedure, plastic flow during the first half of the cut occurs due to unconstrained transient stress redistribution. WRS predictions during the first half of the cut are therefore less accurate compared to the second half, where relatively little plastic flow occurs. For the clamped edge-crack procedure, constrained stress redistribution reduces the level of plasticity in the first half of

the cut but leads to greater plastic flow in the second half. A more distributed loss of measurement accuracy thus exists across the cutting plane, although overall accuracy is greater for clamped edge-crack configuration than for unconstrained edge-crack configuration.

Acknowledgements

Residual stress measurements and weld simulations produced under the auspices of the NeT programme via Task Group 4 have significantly advanced best-practice guidelines for treatment of WRS and post-weld plastic strain, adding considerable value to the present work. The authors are also grateful for insightful discussions regarding computational weld mechanics with Prof. M.C. Smith (University of Manchester) and Dr. P.J. Bendeich (ANSTO).

References

[1] M.B. Prime. Cross-Sectional Mapping of Residual Stresses by Measuring the Surface Contour after a Cut, Journal of Engineering Materials and Technology (2001) 162-168.
[2] M.B. Prime, R.J. Sebring, J.M. Edwards, D.J. Hughes, P.J. Webster. Laser Surface-Contouring and Spline Data-Smoothing for Residual Stress Measurement, Experimental Mechanics 44 (2004) 176 - 184.
[3] G. Johnson. Residual Stress Measurements Using the Contour Method. vol. PhD. Manchester: University of Manchester, 2008.
[4] M.B. Prime, A.T. DeWald. The Contour Method. in: Schajer GS, (Ed.). Practical Residual Stress Measurement Methods. John Wiley & Sons, Ltd., Chichester,WestSussex, UK, 2013.
[5] H.F. Bueckner. Field Singularities and Related Integral Representations, Mechanics of Fracture G.C. Sih, ed. (1973) 239-314.
[6] W. Woo, G.B. An, V.T. Em, A.T. DeWald, M.R. Hill. Through-thickness distributions of residual stresses in an 80 mm thick weld using neutron diffraction and contour method, Journal of Materials Science 50 (2014) 784-793.
[7] R. Simoneau, D. Thibault, J.-L. Fihey. A comparison of residual stress in hammer-peened, multi-pass steel welds – A514 (S690Q) and S4150, Welding in the World 53 (2009) R124-R134.
[8] J. Kelleher, M.B. Prime, D. Buttle, P.M. Mummery, P.J. Webster, J. Shackleton, P.J. Withers. The Measurement of Residual Stress in Railway Rails by Diffraction and Other Methods, Journal of Neutron Research 11 (2003) 187-193.
[9] M.T. Hutchings, P.J. Withers, T.M. Holden, T. Lorentzen. Introduction to the Characterization of Residual Stress by Neutron Diffraction, CRC Press, 2005.
[10] P. Pagliaro, M.B. Prime, J.S. Robinson, B. Clausen, H. Swenson, M. Steinzig, B. Zuccarello. Measuring Inaccessible Residual Stresses Using Multiple Methods and Superposition, Experimental Mechanics 51 (2011) 1123-1134.
[11] M.B. Prime, A.L. Kastengren. The Contour Method Cutting Assumption: Error Minimization and Correction. Proceedings of the SEM Annual Conference. Indianapolis, Indiana, USA: Society for Experimental Mechanics Inc., 2010.
[12] R.J. Dennis, D.P. Bray, N.A. Leggatt, M. Turski. Assessment of the influence of plasticity and constraint on measured residual stresses using the contour method. PVP2012, vol. PVP2008-61490. Chicago, Illinois, USA: ASME Pressure Vessels and Piping Division Conference, 2008.

[13] S.H. Shin. FEM Analysis of Plasticity-induced Error on Measurement of Welding Residual Stress by the Contour Method, Journal of Mechanical Science and Technology (KSME Int. J.) 19 (2005) 1885-1890.
[14] L. Hacini, N. Van Lê, P. Bocher. Evaluation of Residual Stresses Induced by Robotized Hammer Peening by the Contour Method, Experimental Mechanics 49 (2009) 775-783.
[15] P.G. Frankel, P.J. Withers, M. Preuss, H.T. Wang, J. Tong, D. Rugg. Residual stress fields after FOD impact on flat and aerofoil-shaped leading edges, Mechanics of Materials 55 (2012) 130-145.
[16] F. Hosseinzadeh, P. Bouchard. Mapping Multiple Components of the Residual Stress Tensor in a Large P91 Steel Pipe Girth Weld Using a Single Contour Cut, Experimental Mechanics 53 (2012) 171-181.
[17] C. Liu, H.-Y. Zhu, C.-L. Dong. Internal residual stress measurement on inertia friction welding of nickel-based superalloy, Science and Technology of Welding and Joining (2014) 1362171814Y.0000000206.
[18] F. Hosseinzadeh, Y. Traore, P.J. Bouchard, O. Muránsky, Mitigating cutting-induced plasticity in the contour method: Experimental (Part 1), Part 1 of the presnet study (2015).
[19] O. Muránsky, M.C. Smith, P.J. Bendeich, T.M. Holden, V. Luzin, R.V. Martins, L. Edwards. Comprehensive numerical analysis of a three-pass bead-in-slot weld and its critical validation using neutron and synchrotron diffraction residual stress measurements, International Journal of Solids and Structures 49 (2012) 1045-1062.
[20] G.S. Schajer. Practical Residual Stress Measurement Methods, John Wiley & Sons Ltd., 2013.
[21] O. Muránsky, C.J. Hamelin, M.C. Smith, P.J. Bendeich, L. Edwards. The effect of plasticity theory on predicted residual stress fields in numerical weld analyses, Computational Materials Science 54 (2012) 125-134.
[22] O. Muránsky, M.C. Smith, P.J. Bendeich, L. Edwards. Validated numerical analysis of residual stresses in Safety Relief Valve (SRV) nozzle mock-ups, Computational Materials Science 50 (2011) 2203-2215.
[23] Abaqus. Abaqus User's Manual, Version 6.9. SIMULIA, 2008. p.Abaqus User's Manual, Version 6.9.
[24] M.R. Hill. The Slitting Method. in: Schajer GS, (Ed.). Practical Residual Stress Measurement Methods. John Wiley & Sons, Ltd, 2013. pp. 89-108.
[25] F. Hosseinzadeh, M.B. Toparli, P.J. Bouchard. Slitting and Contour Method Residual Stress Measurements in an Edge Welded Beam, Journal of Pressure Vessel Technology 134 (2012) 011402-011406.
[26] Y. Traore, S. Paddea, P. Bouchard, M. Gharghouri. Measurement of the Residual Stress Tensor in a Compact Tension Weld Specimen, Experimental Mechanics 53 (2013) 605-618.
[27] F. Hosseinzadeh, J. Kowal, P.J. Bouchard. Towards good practice guidelines for the contour method of residual stress measurement. The Journal of Engineering: Institution of Engineering and Technology, 2014.

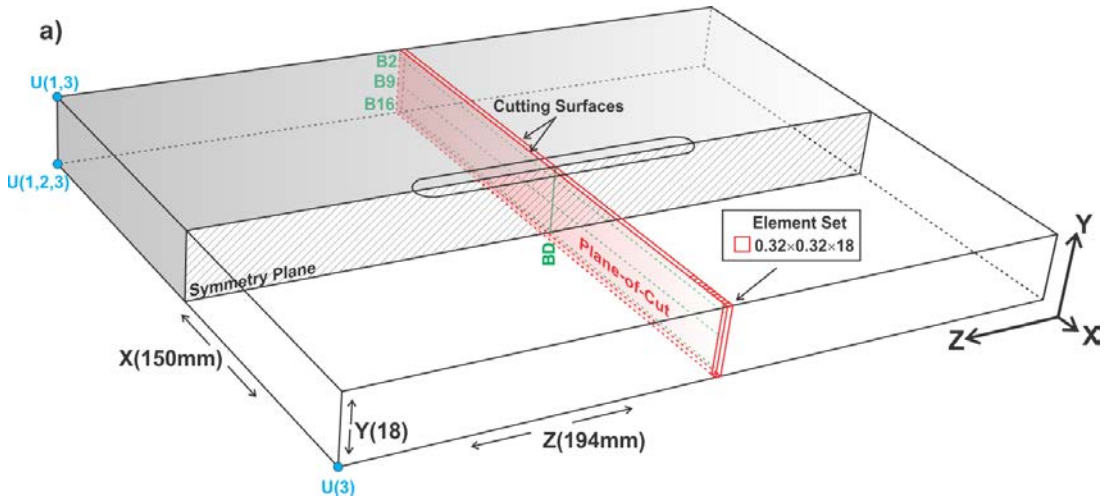

Fig. 1a: Schematic of the NeT TG4 benchmark specimen, and its representation for numerical FE analyses. X = transverse direction; Y = normal direction; Z = longitudinal direction. Note that the initial welding analysis used a half-model (the shaded region shown), while the contour cutting models use a full 3D FE mesh (b). Planar sectioning of the model is performed along the plane-of-cut, which is comprised of a series of element sets with an assumed cut thickness of 0.32 mm. In cases where clamping is not used, a set of pin constraints to prevent rigid body rotation is applied to the model (shown here by blue dots). Lines (in green) highlight the nominal location of cross-weld stress profiles taken using neutron and synchrotron diffraction techniques [19].

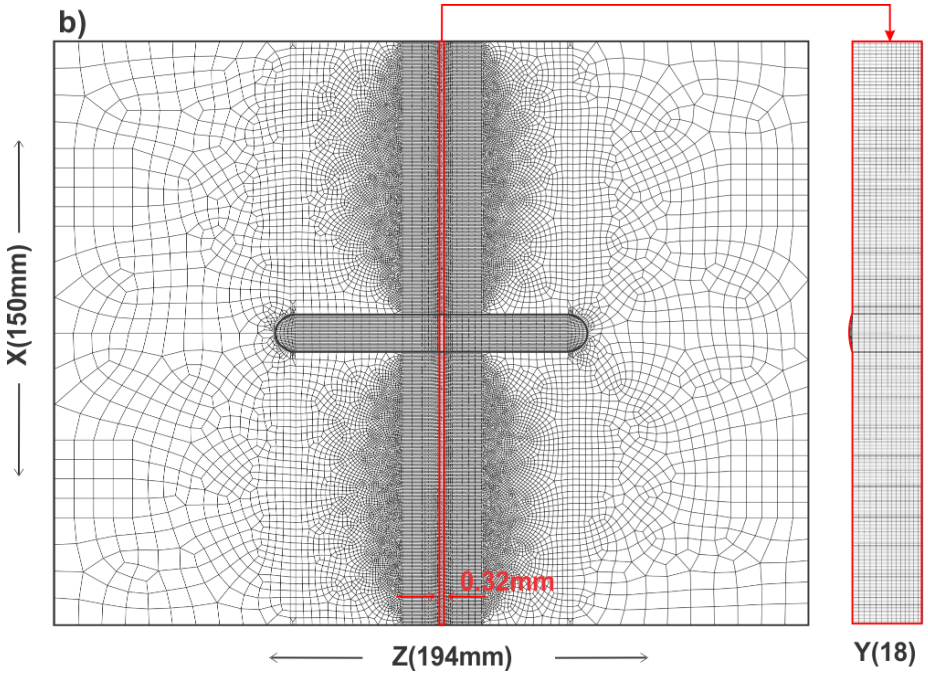

Fig. 1b: The mesh of the contour cutting model, comprising 396,626 hexahedral quadratic elements with reduced integration (ABAQUS designation C3D20R). The mesh was significantly refined along the plane-of-cut as well as the through the plate thickness relative to the weld model [19].

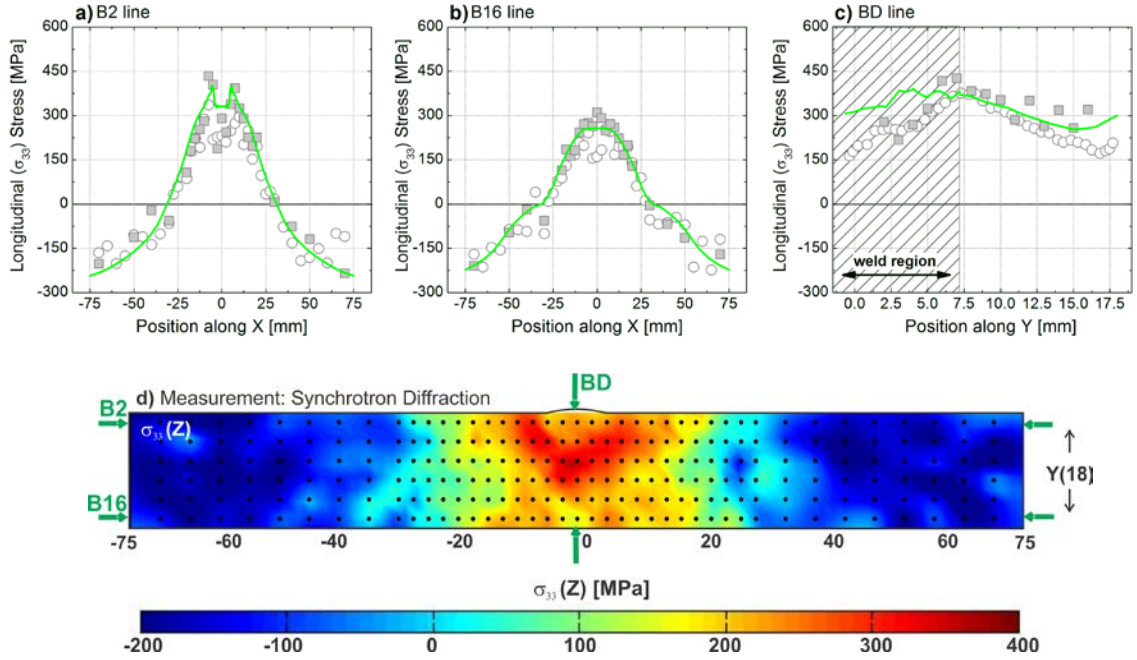

Fig. 2: Longitudinal (σ_{33}) WRS measured in the NeT TG4 benchmark weld specimens. A set of cross-weld stress profiles are shown (see Fig. 1a for profile locations) along: (a) the B2 line, 2 mm under the plate top surface; (b) the B9 line, 9 mm under the plate top surface; and (c) the BD line, along the sample thickness at the centre of the plate. FE half-model predictions are mirrored about the weld centreline to compare with experimental measurements. The error bars (approximately 40 MPa) for both measurement techniques have been omitted for clarity. The full set of diffraction data is presented in Ref. [19, 21]. Subfigure (d) presents synchrotron X-ray measurements of the original (pre-cutting) longitudinal WRS in the as-welded NeT TG4 benchmark weld specimen on the plane of interest (i.e. plane-of-cut in the contour method).

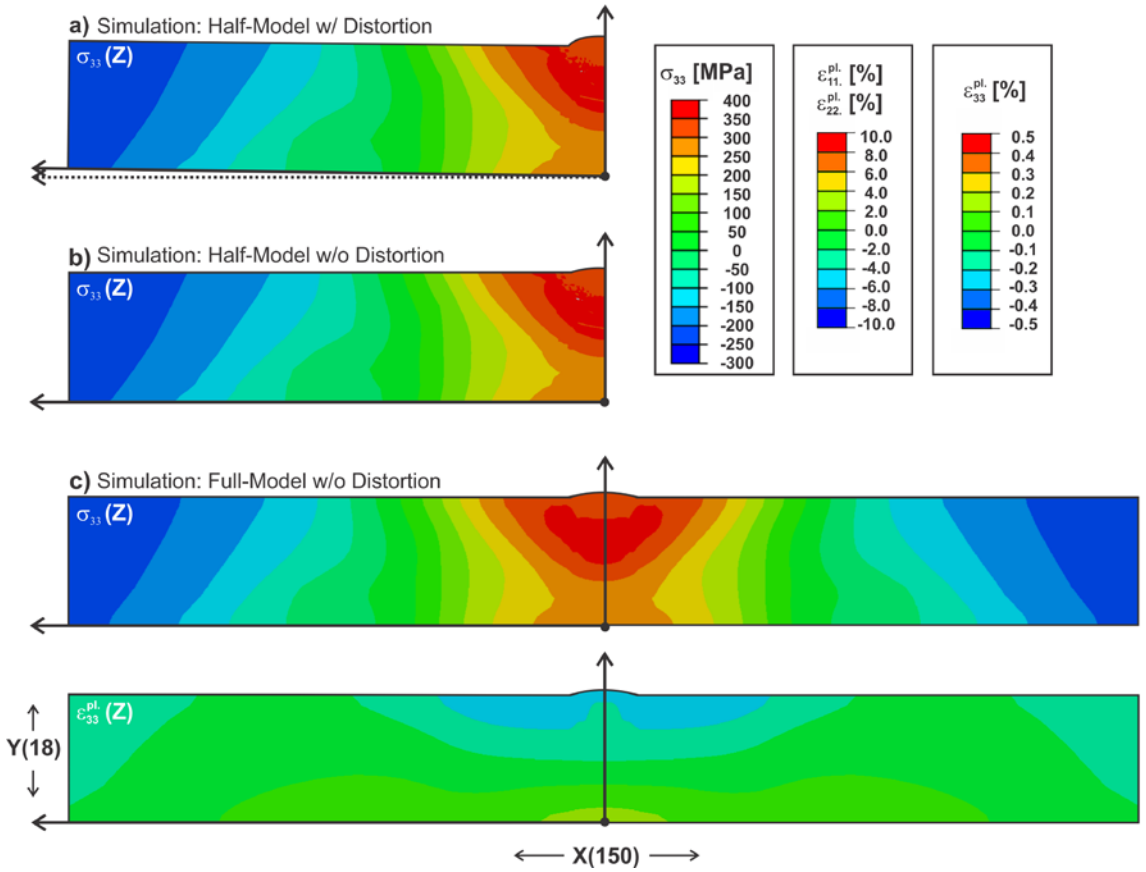

Fig. 3: Mapping procedure used to transfer the results from the weld FE model to the contour cutting FE model: (a) the original weld half-model is distorted due to the spatial distribution of the WRS field; (b) this distortion is removed by running an additional analysis step that does not record nodal displacement; and (c) predictions from the weld model are then transferred and mirrored onto the full 3D contour model.

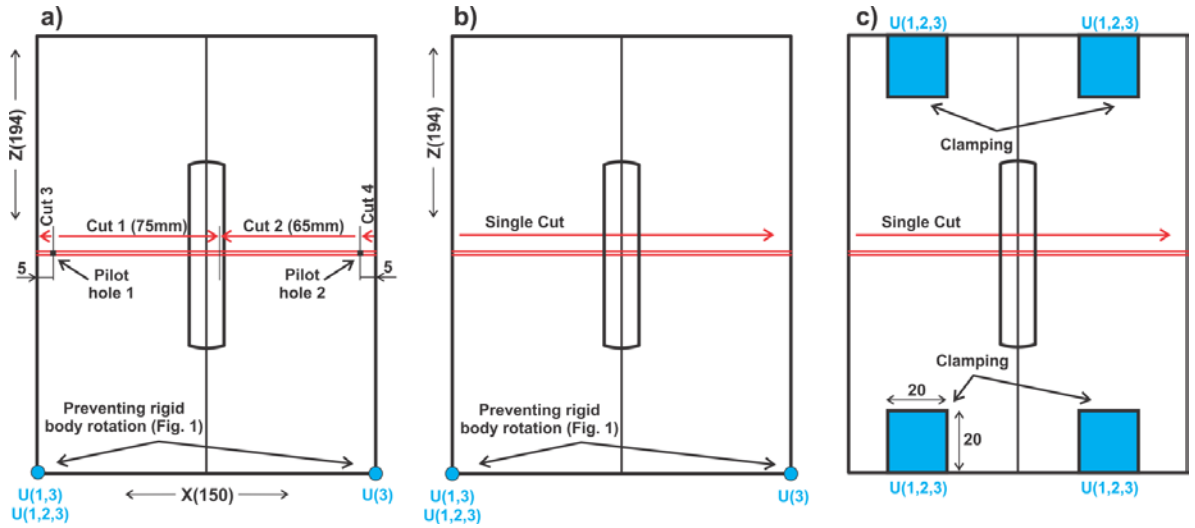

Fig. 4: Different cutting strategies investigated: (a) the double-embedded cutting configuration; (b) an edge-crack configuration with minimal constraint to prevent rigid-body rotation; and (c) an edge-crack configuration with conventional clamping restraints.

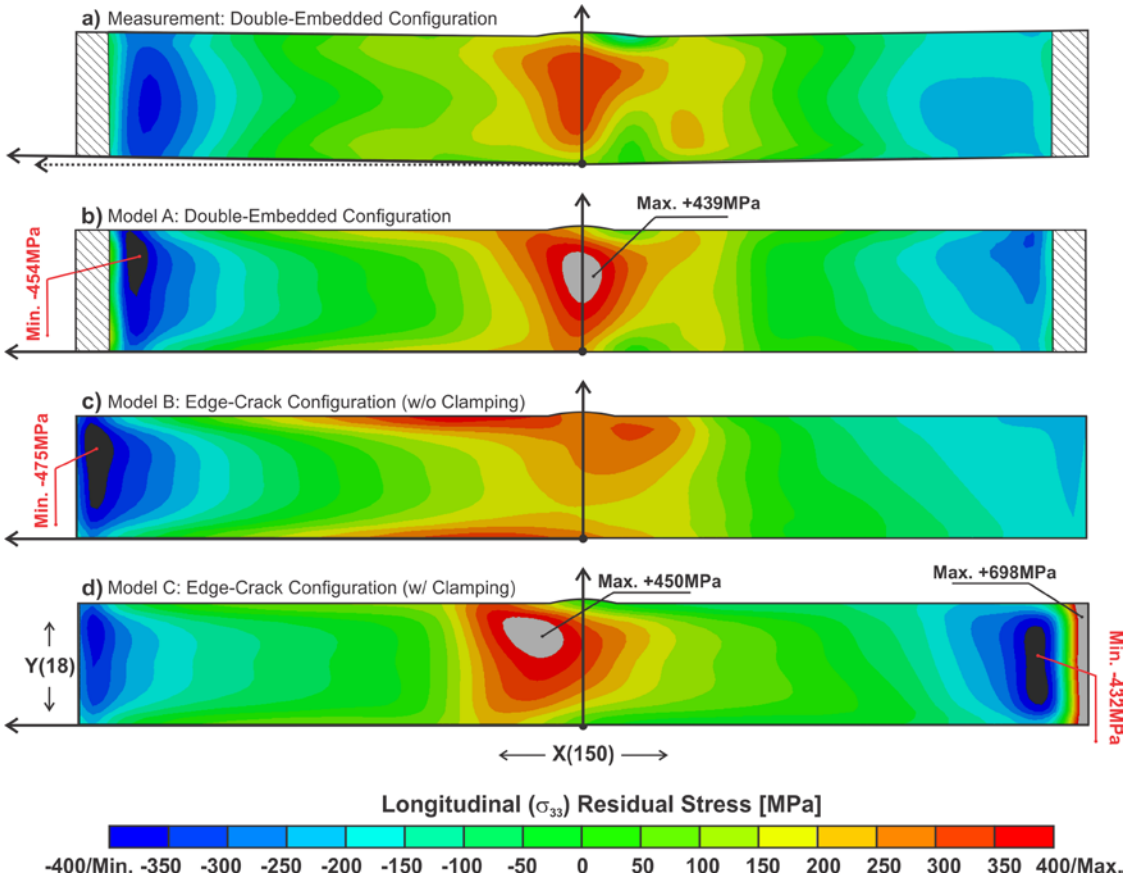

Fig. 5: Comparison of predicted longitudinal (σ_{33}) WRS along the cutting plane after different contour cutting strategies: (a) measured WRS using the double-embedded cutting configuration; (b) predicted WRS using the double-embedded cutting configuration; (c) predicted WRS using the edge-crack configuration with no restraint; and (d) predicted WRS using the edge-crack configuration with clamping. The efficacy of the cutting configurations in (b-d) can be determined by comparing these post-cutting residual stress against the pre-cutting residual stress solution from the NeT TG4 weld model (Fig. 3c).

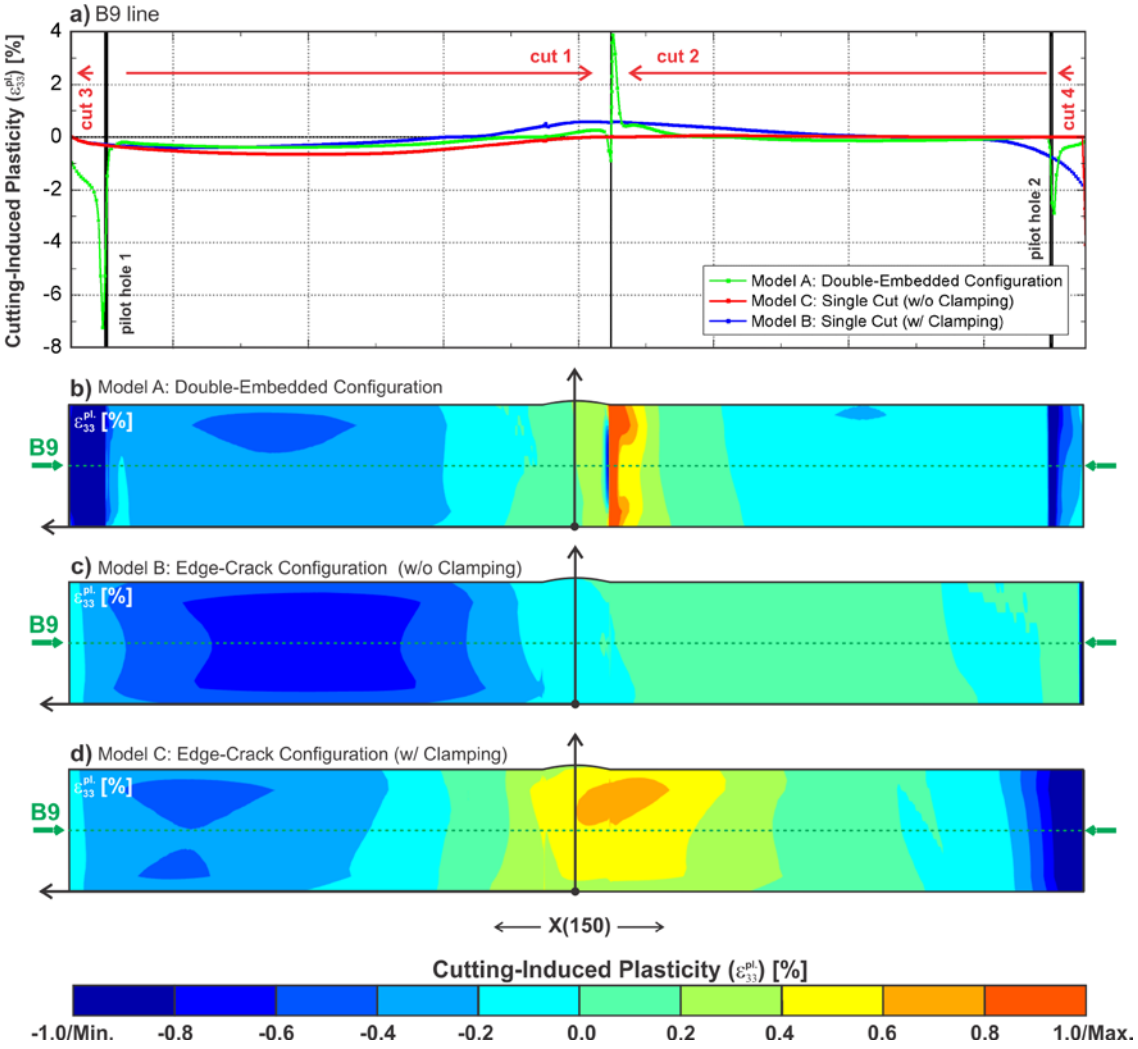

Fig. 6: Comparison of the predicted cutting-induced longitudinal plastic strain ($\varepsilon_{33}^{pl.}$) along the cutting plane after different contour cutting strategies: (a) line profiles of the cutting-induced plasticity predicted for each technique, along the B9 line shown in Fig. 1a; (b) $\varepsilon_{33}^{pl.}$ when using the double-embedded cutting configuration; (c) $\varepsilon_{33}^{pl.}$ when using the edge-crack configuration with no restraint; and (d) $\varepsilon_{33}^{pl.}$ when using the edge-crack configuration with clamping. The original welding-induced plastic strain (shown in Fig. 3d) has been removed from this data. The lower-bound plastic strain is lower than -1.0% and the upper-bound plastic strain is greater than 1.0 % in (b); common strain limits were chosen to directly compare strain fields predicted in Model A with those predicted in Models B and C. For clarity, the magnitudes of these upper-bound strains are captured in $\varepsilon_{33}^{pl.}$ profiles shown in (a).

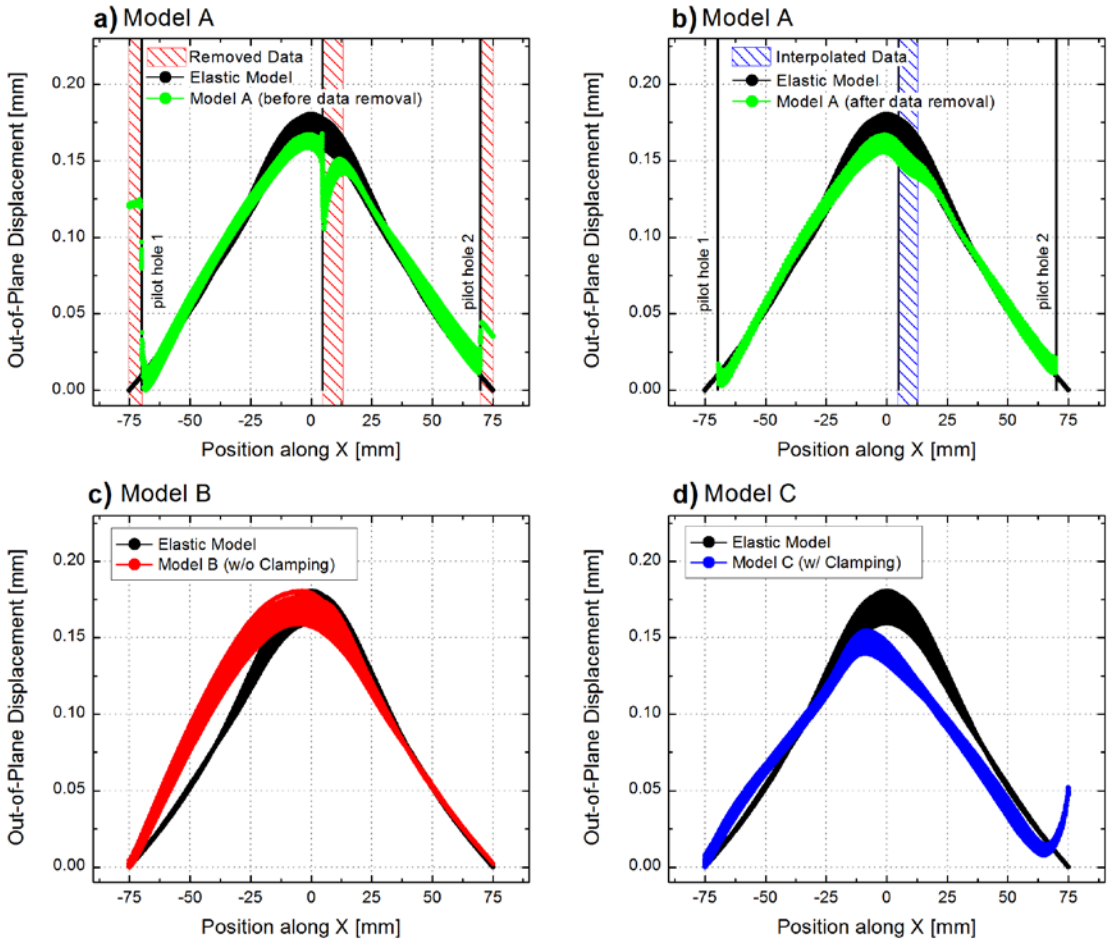

Fig. 7: Comparison of the averaged (over both cutting surfaces) out-of-plane displacment as predicted by (a,b) Model A, (c) Model B and (d) Model C, against the out-of-plane displacment predicted by an idealised fully elastic cutting simulation. Subfigure (a) shows predicted out-of-plane displacment before removal of the localised displacments caused by cutting-induced plasticity, while (b) shows the same out-of-plane displacment after removal of these localised features and data interpolation is performed. Note that this post-processed out-of-plane displacement was then applied in the back-calucation of WRS for Model A (Fig. 5b).